Few-Body Syst (2024) 65:82
https://doi.org/10.1007/s00601-024-01952-y

Piotr Froelich · Takuma Yamashita · Yasushi Kino · Svante Jonsell · Emiko Hiyama

Formation of the Positronium Antihydride Molecules ($\bar{H}Ps$) in Low Energy, 5-Body Collisions of Antihydrogen Ion $\bar{H}^+$ with Positronium Atoms Ps

Received: 22 January 2024 / Accepted: 1 August 2024

Abstract In this paper we present the first pilot calculation of the elastic and inelastic cross sections for the 5-body scattering of antihydrogen ions with positronium atoms. These cross sections have not been calculated before and are not known experimentally. In particular, we focus on the collisional rearrangement reactions $\bar{H}^+ + Ps \rightarrow \bar{H}Ps + e^+$ which deplete the $\bar{H}^+$ ions and result in stable atomcules $\bar{H}Ps$. To better understand the mechanism of this rearrangement, we study the 3-dimensional, angle resolved positron densities of the 3- and 4-body fragments in the initial and final states of the rearrangement collision.

1 Introduction

The system consisting of positronium (Ps) and antihydrogen ($\bar{H}$) atoms is known to exist in only one bound state of the positronium antihydride ($\bar{H}Ps$) which is a hybrid atomcule that possesses both atomic and molecular properties [1–3]. $\bar{H}Ps$ cannot be formed in purely 2-body $\bar{H} + Ps$ collisions, but it can be obtained when Ps collides with the antihydrogen ion $\bar{H}^+$

$$\bar{H}^+ + P_s \rightarrow \bar{H}P_s + e^+ \tag{1}$$

whereby the binding energy is conveyed to the ejected positron.

The here presented calculations of the cross sections for reaction (1) have been done having in mind the large scale experiments with antihydrogen atoms and ions at CERN [4–7]. However the present calculations may become interesting in a broader perspective, since they are applicable to collisions with charge-conjugated

P. Froelich (✉)
Department of Chemistry, Uppsala University, Box 523, 751-20 Uppsala, Sweden
E-mail: piotr.froelich@kemi.uu.se

T. Yamashita
Institute for Excellence in Higher Education, Tohoku University, Sendai, Miyagi 980-8576, Japan

T. Yamashita · Y. Kino
Department of Chemistry, Tohoku University, Sendai, Miyagi 980-8576, Japan

S. Jonsell
Department of Physics, Stockholm University, 10691 Stockholm, SE, Sweden

E. Hiyama
Department of Physics, Tohoku University, Sendai, Miyagi 980-8578, Japan

E. Hiyama
Nishina Center, RIKEN, Wako, Saitama 351-0198, Japan

Published online: 19 August 2024

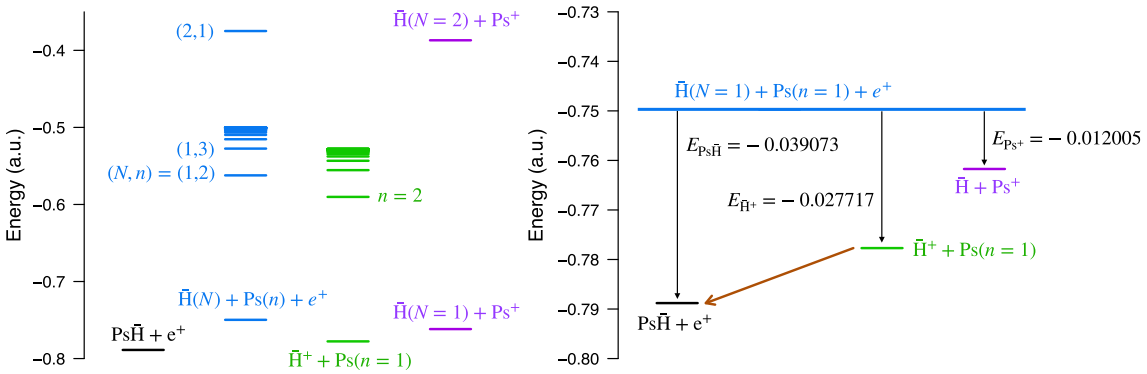

Fig. 1 Left frame: the energy thresholds of the 5-body system $Ps\bar{H}^+$. Shown are the internal energy levels of the whole system being split into indicated fragments. Right frame: magnification of the energy region below the 3-body break-up. The arrow indicates the rearrangement reaction of interest, Eq. (1)

fragments (e.g. in $H^- + Ps$ collisions) which do not contain antiprotons, so that experiments can be done without access to large accelerators and decelerators such as those at CERN.

The interest in the collisional reaction (1) stems from the fact that the $\bar{H}^+$ ions are amenable to sympathetic cooling (notably in ion Coulomb crystals) and, after photo-detachment of one positron, result in ultra-cold antihydrogen atoms that are to be used in ballistic experiments testing the gravitational interaction between matter and antimatter. The ongoing GBAR experiment at CERN works on the production of $\bar{H}^+$ ions in $\bar{H} + Ps \rightarrow \bar{H}^+ + e^-$ collisions [4–7]. In this context the reaction (1) is a scavenging process that depletes the newly formed $\bar{H}^+$ ions that pass the positronium target chamber.

Reaction (1) belongs to the class of notoriously difficult quantum-mechanical few body problems that defy non-numerical solutions. Over years many methods have been developed to approach this type of problems, we mention the most relevant ones. They go back to the Faddeev (F) solution of the 3-body problem [8] and the following Faddeev-Yakubovsky (F-Y) extension for 4 and more particles [9], which is widely used today. The Alt-Grassberger-Sanhas (AGS) method converts the problem to Lippmann-Schwinger-type equations for transition operators in momentum space [10]. Other approaches attempt to solve the Schrödinger equation for the total scattering wave function in configuration space combining the variational methods with the coupled channel equations, e.g. using Hyperspherical Harmonics (HH) and Kohn variational method [11], or Gaussian Expansions Method and Ritz variational method [12]. Recent advances in the field are driven by applications to nuclear and cold atom physics [13–16].

The collisional reaction (1) presents a 5-body problem that we reduce to the 4-body problem and solve exactly using the technique of Gaussian Expansion Method (GEM) combined with the coupled rearrangement channels (CRC) method. The scattering matrix **S** and the cross sections are obtained from the coupled, non-local integro-differential equations that explicitly couple all open channels. The distinctive novel feature of our approach is the simultaneous use of several Jacobi sets of coordinates in the expansion of the multi-channel wave functions. That allows efficient and rigorous treatment of the scattering cross sections.

The GEM method has been previously successfully applied to the stationary 3, 4 and 5 body problems in nuclear physics [17,18] to 3 and 4 body problems in atomic and molecular physics [19,20], and to the combinations thereof [20,21]. The GEM/CRC method has been used to 3 and 4 body scattering problems [21–23]. For the reviews see [24,25]. In the present paper we have applied this method to calculate the so far unknown cross sections for the 5-body collisional rearrangement reaction (1) that depletes $\bar{H}^+$ ions and results in the $\bar{H}Ps$ molecules.

We discuss the near-threshold features of the scattering cross sections and show that they comply with the expected behaviour stipulated by the Wigner's law. We also visualize, via the probability density plots, the mechanism of the rearrangement reaction (1) whereby $\bar{H}^+$ shrinks and gets more tightly bound by capturing the electron, while the positron carries away the excess of energy.

2 The Mechanism of the Reaction $\bar{H}^+ + Ps \rightarrow \bar{H}Ps + e^+$

We start by considering the relevant energy thresholds of the collision (1). Figure 1 shows the energy levels of the 5-body system consisting of an antiproton, 3 positrons and 1 electron, from the point of view of various clusterings of the system. The energy levels of these clusterings (shown in different colours) give us a general map of the possible outcomes of the $\bar{H}^+ + Ps$ scattering. The black level shows the energy of the $\bar{H}Ps$ atomcule ($E = -0.788870$). We notice that it is below the energy of $\bar{H}^+ + Ps(n = 1)$ (lowest green level). Thus the reaction (1) is exothermic. The arrow shows the energy release resulting from the formation of $\bar{H}Ps$ in collisions of $\bar{H}^+$ with the positronium in the ground state $\bar{H}^+ + Ps(n = 1) \rightarrow \bar{H}Ps + e^+$.

In the following we will consider the $\bar{H}^+ + Ps(n = 1)$ collisions with energy below the 3-body break-up. In such a case only three channels are open: elastic scattering, reaction to $\bar{H}Ps + e^+$ or reaction to $\bar{H}(n = 1) + Ps^+$. The right panel of Fig. 1 shows the situation in magnification.

2.1 Disintegration of $\bar{H}^+$ via Electron Transfer

Looking at Eq. (1) gives an intuitive impression that $\bar{H}^+$ binds the electron harder than the positron does in Ps. Lets investigate how the $\bar{H}^+$, upon accepting an electron from Ps, generates the binding energy that is partly passed to the expelled positron in the reaction (1). This binding energy is due to the combined effect of the electron interacting with the antiproton and with the positron cloud (of 2 positrons), affecting the latter. Thus we expect that $\bar{H}^+$ undergoes a structural change while accommodating (binding) the electron. We will illustrate this change by comparing the positron densities of $\bar{H}^+$ (before the electron transfer) and in $\bar{H}Ps$ (i.e. after the electron transfer). To accomplish that, we introduce the 3-dimensional, angle resolved probability densities that are defined as

$$P_c(r_c, R_c; \theta_c) = N r_c^2 R_c^2 \int d\rho_c d\hat{\tau}_c \Psi^* \Psi \tag{2}$$

where, for the system of n particles, Ψ is the $3(n-1)$ dimensional wave function of the system written in Jacobi coordinates given by vectors $\mathbf{r}_c$, $\mathbf{R}_c$ and ρ_c (see Fig. 2). The integration $d\hat{\tau}_c$ is over $3(n-2)$ dimensions leaving distances r_c, R_c and the angle $\theta_c = \arccos(\hat{\mathbf{r}}_c \cdot \hat{\mathbf{R}}_c)$ between them. The calculation of the wave functions Ψ is presented in Sect. 2.3, but we first discuss the various Jacobi coordinates $\mathbf{r}_c$, $\mathbf{R}_c$ and ρ_c used in its construction.

2.2 Jacobi Coordinates

For $\bar{H}Ps$ there are 15 possible ways to choose the Jacobi coordinates (c=1,2,... 15). We use 11 of them (see Fig. 2) in the expansion of the wave function Ψ for $\bar{H}Ps$. In expansion of the wave function for $\bar{H}^+$ we use all (5) possible arrangements. The Jacobi arrangements occur in pairs, with the positrons exchanged, as to assure the proper permutation symmetry of the wave function. These pairs are indicated on Fig. 2 by the two-headed arrow $\leftrightarrow$ that symbolizes the permutation operation; they are presented in two leftmost panels of Fig. 2. The arrangements that contain the coordinate directly connecting two positrons are not permuted, since they stay invariant upon the permutation operation (up to the sign). They are presented in the rightmost panel of Fig. 2.

Some of the arrangements are more suitable than others in the description of a particular clustering of the system. For example, the natural Jacobi set for the description of the initial channel would be c=1 (and its positron-permuted counterpart c=2) where the CM of $\bar{H}^+$ is connected with the CM of the Ps atom. The natural Jacobi set for the final state could be c=3 (and its positron-permuted counterpart c=4) where the CM of $\bar{H}Ps$ is connected with the departing positron. Still another arrangements (c=5 $\leftrightarrow$ c=6 and c=8) are suitable for the $\bar{H} + Ps^+$ clustering which constitutes a viable open channel. We also include the Jacobi arrangements suitable for description of the break-up tendency of the system, with coordinates connecting particles of the same charge (viz. c=7 and c=9 in the most right panel on Fig. 2).

The presence of coordinates conforming with the initial and final states of reaction (1) is certainly important, but we should have a more holistic look at this process. We realize that the kinetic energy released by the electron is very small, only -0.011424 a.u. This energy is only a small fraction (around 4%) of the binding energy released by the destructed positronium. Hence almost all binding energy of Ps atom is absorbed by $\bar{H}Ps$ and is redistributed through intricate correlations involving all 4 particles. For that reason, in the construction of the scattering wave functions we include all possible Jacobi arrangements, as to assure comprehensive description of the correlations in the important reaction region.

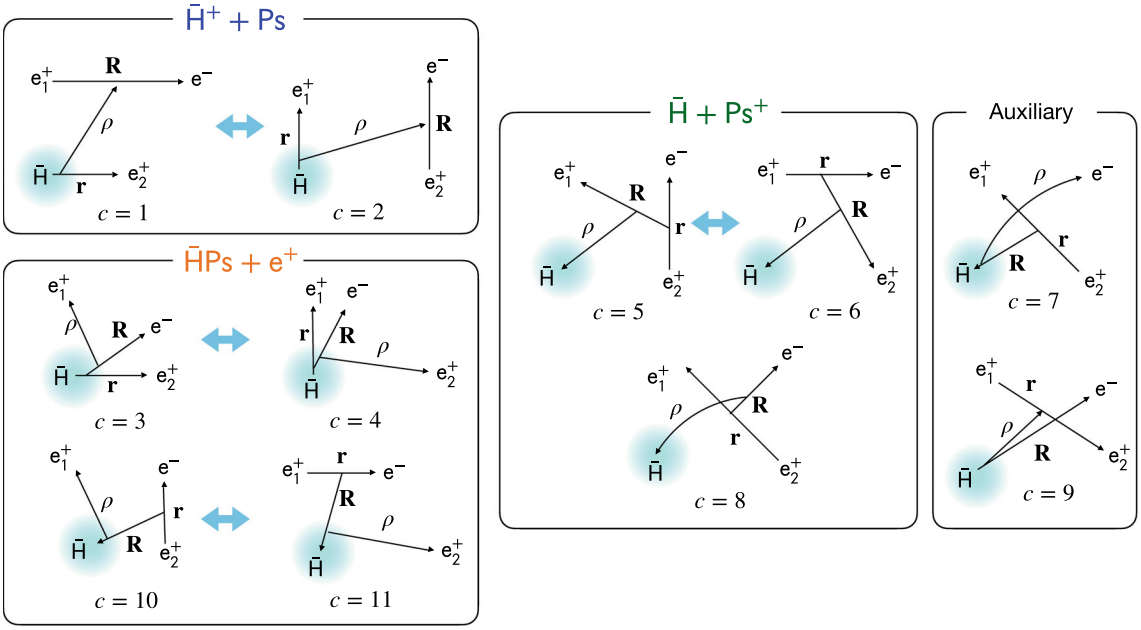

Fig. 2 The Jacobi coordinates used in this work. The two-headed arrows ↔ symbolize the positron permutation operation. The panels collect the Jacobi arrangements particularly suitable for description of the indicated clusterings of the system, corresponding to various reaction channels

2.3 The GEM Approach to the Few-Body Problem

The collisional reaction (1) constitutes a 5-body scattering problem. When choosing the method for its treatment it is useful to understand the internal structure of the fragments, especially since both $\bar{\mathrm{H}}^+$ in the initial state and $\bar{\mathrm{H}}\mathrm{Ps}$ in the final state are highly correlated 3 and 4 body systems. Because of that, we have used the Gaussian Expansion Method (GEM) that has been shown to be very effective and accurate in the treatment of 3, 4 and 5-body bound and resonant states [19,24]. The method has been recently advanced in two directions: extension allowing treatment of the 6-body stationary problems and, importantly for the present work, extension allowing treatment of the 4-body *scattering* problems [22,23].

We first discuss the construction of the wave functions for the stable fragments of the collision (1) as to get insight into reaction mechanism through the analysis of the probability densities (2); the formulation of the scattering problem will be presented in Sect. 5.

The 3- and 4-body fragments of reaction (1) (i.e. $\bar{\mathrm{H}}^+$ and $\bar{\mathrm{H}}\mathrm{Ps}$) exist each in only one bound state (spin singlet with the internal angular momentum $\mathcal{L} = 0$). Within the GEM, the wave functions for these fragments are obtained variationally, as ground state solutions to the Schrödinger equation in matrix form. The variational wave function for the 4-body fragment is written as

$$\Phi_v = \frac{(1+\mathcal{P})}{\sqrt{2}}\Big\{\sum_c \sum_{L_c,l_c,\lambda_c} \sum_{N_c,n_c,\nu_c} a^{(v)}_{\{c\};\{L_c,l_c,\lambda_c\};\{N_c,n_c,\nu_c\}} G(R_c;\, L_c,\, R_{N_c}) g(r_c;\, l_c,\, r_{n_c}) \gamma(\rho_c;\, \lambda_c,\, \rho_{\nu_c}) \times \\ \times\, [[Y_{L_c}(\hat{\boldsymbol{R}}_c) Y_{l_c}(\hat{\boldsymbol{r}}_c)] Y_{\lambda_c}(\hat{\boldsymbol{\rho}}_c)]_{JM}\Big\} \tag{3}$$

In the above equation $G(R_c)$, $g(r_c)$ and $\gamma(\rho_c)$ are gaussian functions of Jacobi coordinates R_c, r_c and ρ_c, respectively,

$$G(R_c;\, L_c,\, R_{N_c}) g(r_c;\, l_c,\, r_{n_c}) \gamma(\rho_c;\, \lambda_c,\, \rho_{\nu_c}) = R_c^{L_c} e^{-(\frac{R_c}{R_{N_c}})^2} r_c^{l_c} e^{-(\frac{r_c}{r_{n_c}})^2} \rho_c^{\lambda_c} e^{-(\frac{\rho_c}{\rho_{\nu_c}})^2}, \tag{4}$$

$Y_{L_c}(\hat{\boldsymbol{R}}_c)$, $Y_{l_c}(\hat{\boldsymbol{r}}_c)$, and $Y_{\lambda_c}(\hat{\boldsymbol{\rho}}_c)$ are the corresponding spherical harmonics, coupled to the total angular momentum J, and $a^{(v)}_{\{c\};\{L_c,l_c,\lambda_c\};\{N_c,n_c,\nu_c\}}$ are the expansion coefficients, determined variationally. The summation over c indicates that the expansion is written in 11 different Jacobi coordinate arrangements (see Fig. 2). The summation over L_c, l_c, λ_c runs over the angular momenta included in each Jacobi arrangement c, and the

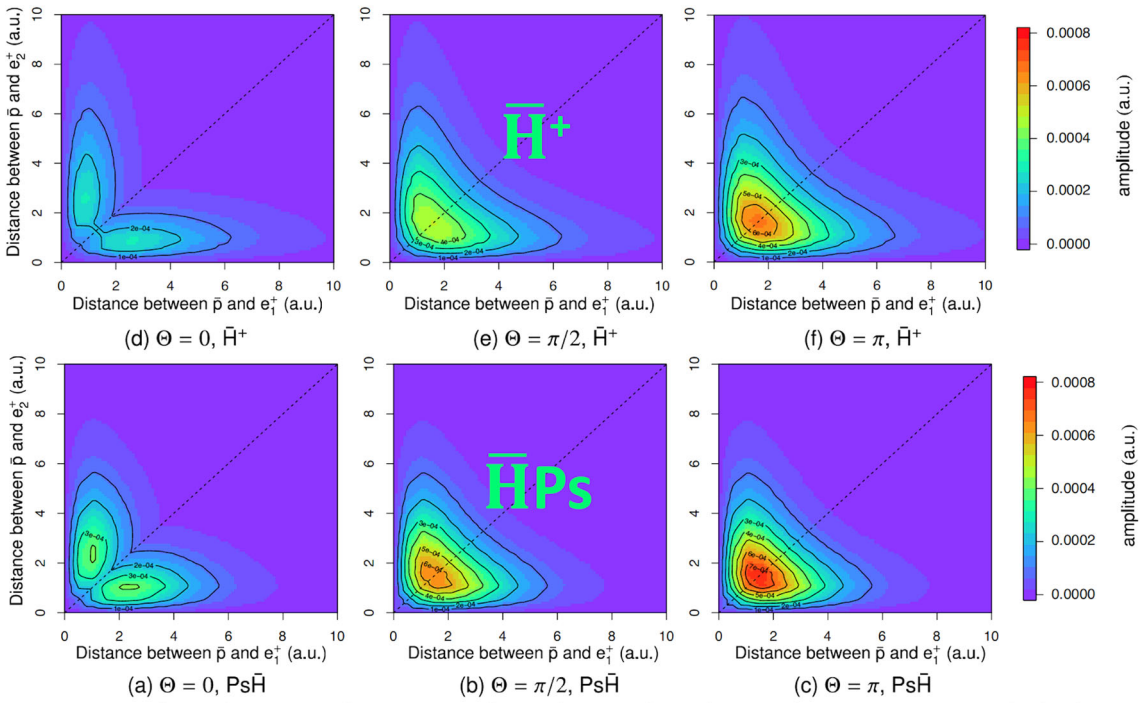

Fig. 3 The 3-dimensional, angle resolved positron probability density for a free $\bar{H}^+$ (upper row) and $\bar{H}$Ps (lower row). The colored contours show the probability of finding the two positrons at distances R and r from the antiproton, while keeping angle $\theta = \arccos(\hat{\mathbf{r}} \cdot \hat{\mathbf{R}})$ between their respective vector positions. The actual coordinates of the figure panels are $R = R_3$, $r = r_3$ and $\theta = \theta_3$, the angle between $\mathbf{r}_3$ and $\mathbf{R}_3$ vectors of the Jacobi coordinate arrangement $c = 3$ (see Fig. 2). We see that the positron density of $\bar{H}$Ps looks very much like that of a free $\bar{H}^+$, rendering a picture of $\bar{H}^+$ being embedded in $\bar{H}$Ps. We note that for all θ values the density is increased when one of the positrons is closer to the antiproton then the other, $R < r$ or $R > r$. With the increase of angle θ, the two separate density islands take form of two elongated ridges meeting at the summit at $R = r$. We also note that, somewhat counterintuitively, the density of $\bar{H}^+$ embedded in $\bar{H}$Ps (second row) is more compact than for a free $\bar{H}^+$ (upper row)

summation over N_c, n_c, ν_c runs over gaussian functions used for expansion in each arrangement c and given L_c, l_c, or λ_c. The last summation dictates the number of gaussian functions used for each $\{c, L_c\}, \{c, l_c\}, \{c, \lambda_c\}$ combination, and the effective extension of these gaussians (through the non-linear coefficients $R_{N_c}, r_{n_c}, \rho_{\nu_c}$). The symbol $\mathcal{P}$ in front of the summations stands for the positron permutation operator. The three body wave function for $\bar{H}^+$ has the analogue construction restricted to $\mathbf{r}_c, \mathbf{R}_c$.

3 Positron Densities of $\bar{H}^+$ and $\bar{H}$Ps

Using the wave functions for the collisional fragments calculated as described above we are able to discuss their structure. In particular we are interested to compare the positron densities of $\bar{H}^+$ and $\bar{H}$Ps that appear in the initial and final states of reaction (1). We form the densities according to the definition given in Eq. (2) in the Jacobi arrangement $c = 3$, presented in Fig. 2. Because the collisional center of mass is close to the antiproton, the Jacobi coordinates $\mathbf{R_3}$ and $\mathbf{r_3}$ can be understood to represent the positions of the two positrons with respect to the antiproton $\bar{p}$. Figure 3 shows the positronic probability density $P_3(r_3, R_3; \theta_3)$ for free $\bar{H}^+$ in the initial channel (first row), and the similar density for $\bar{H}$Ps in the final channel (second row).

As is seen, the positron density is more compact in the second row - for $\bar{H}^+$ that binds an electron forming $\bar{H}$Ps. Regarding the rearrangement process (1) we conclude that $\bar{H}^+$ captures the electron from Ps whereby it shrinks and gets more tightly bound.

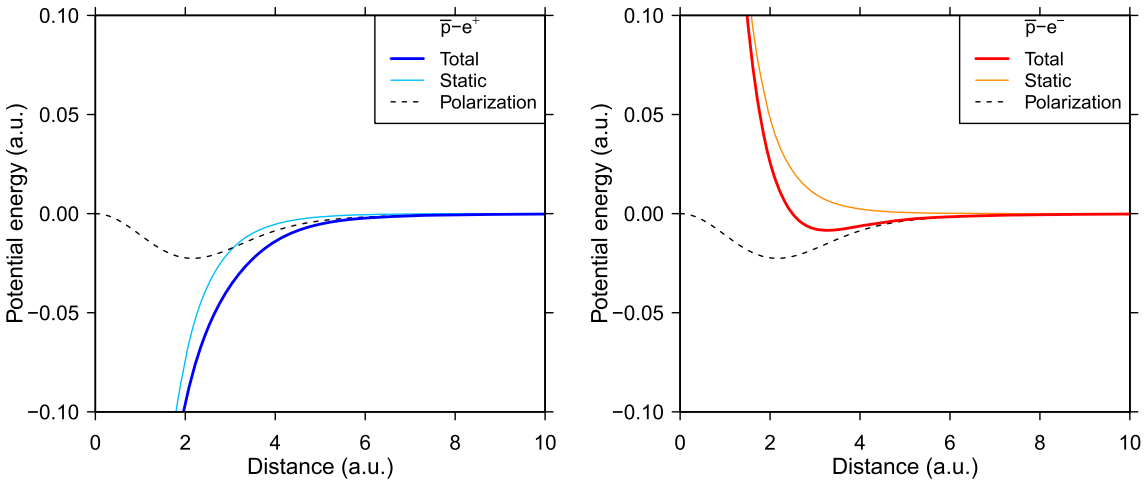

Fig. 4 The effective potentials. Left panel: $V_1(r) = V_2(r)$ for the positrons interacting with the core. The dark blue line is the combination of the static potential (light blue) and the polarization potential (broken line). Right panel: $V_3(r)$ for the electron interacting with the core. The red line is the combination of the static potential (orange) and the polarization potential (broken line)

4 The Frozen Core Approach

Inspection of the positron probability densities presented in Fig. 3 suggests that considerable part of the system's positronic density is in the "unequal arms" configuration, in which one of the positrons is closer to the antiproton than the other. We utilize this observation in formulation of the scattering problem, by treating the antiproton and one of the positrons as the $\bar{\mathrm{H}}$ subcluster that interacts with the remaining leptons via effective potentials. Figure 2 shows the situation with one of positrons being part of the $\bar{\mathrm{H}}$. As Fig. 2 indicates, the five body problem can be converted to the 4-body problem in which the $\bar{\mathrm{H}}$ interacts with the remaining leptons via effective interactions, and the leptons interact with each other with Coulomb interactions. This type of approach has been successfully used before to treat collisions of positrons with alkali atoms [26–30].

In our case of reaction (1) the effective interactions contain a term which acts as a screened Coulomb potential and another term which describes the polarization of the core by the lepton. At short range, the effective interaction should be Coulomb attractive for the positron, and Coulomb-repulsive for the electron, but the polarization interaction is attractive for both types of leptons. Thus for the positron we have

$$V_1(r) = -\frac{\exp(-r\nu_1)}{r} - \frac{\alpha}{2}V_p(r) \tag{5}$$

and for the electron

$$V_3(r) = +\frac{\exp(-r\nu_3)}{r} - \frac{\alpha}{2}V_p(r) \tag{6}$$

where r is the distance from the lepton to the antiproton, $\alpha = \frac{9}{2}$ is the polarizability of the $\bar{\mathrm{H}}$ atom [31] and ν_1, ν_3 are adjustable parameters. The polarization potential $V_p(r)$ has the form

$$V_p(r) = \frac{1}{r^4}\left\{1 - \exp\left[-\left(\frac{r}{d}\right)^6\right]\right\} \tag{7}$$

where d is an adjustable parameter related to the size of the subcluster being polarized. This form of $V_p(r)$ assures that it emerges gradually at distances larger than the size of $\bar{\mathrm{H}}$ and vanishes as $r \to 0$. For practical purposes (to avoid numerical integration of matrix elements) the polarization potential is expanded in terms of Gaussian functions. We have confirmed that the expanded potential reproduces the exact r^{-4} trend to at least 100 bohrs.

The interaction of the second active positron with the core is the same as for the first positron, $V_1(r) = V_2(r)$. The effective potentials have the desired property that they act like Coulomb interaction at short distances to

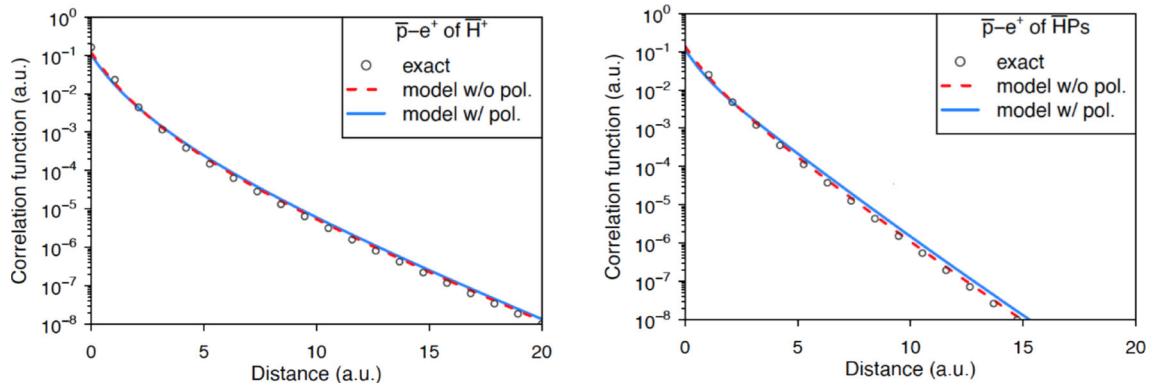

Fig. 5 The 1-dimensional probability density $C(r_{\bar{p}e^+})$ for finding a positron at the distance $r_{\bar{p}e^+}$ from the antiproton. The circle-lines show the probability densities obtained from the exact 3-body solution for $\bar{H}^+$ (left panel) and from the exact 4-body solution for $\bar{H}$Ps (right panel). The other lines show the same probability density obtained with the core potential that includes the polarization term (solid line), and without the polarization (dashed line). We see that the densities obtained with the effective potentials are nearly identical to those obtained from the exact 3- and 4-body wave functions

the antiproton (inside the positron cloud), but at large distances the leptons interact with the $\bar{H}$ (core) via polarization potential $-\frac{\alpha}{2}\frac{1}{r^4}$

$$V_1(r \to 0) \propto -\frac{1}{r}, \qquad V_1(r \to \infty) \propto -\frac{\alpha}{2}\frac{1}{r^4}. \tag{8}$$

The core potentials are optimized as to deliver the exact binding energy of the subclusters of the 5-body system, notably for the antihydrogen ion $\bar{H}^+$ (in the initial state) and positronium antihydride $\bar{H}$Ps (in the final state). We first determine the interaction V_1 of the core with the positron by tuning the binding energy of the two-body problem to the exact 3-body energy of the antihydrogen ion $\bar{H}^+$ that appears in the initial state. Then, using fixed $V_1 = V_2$ we determine the interaction V_3 of the electron with the core by tuning the binding energy of the 3-body problem (core, e^+, e^-) to the exact 4-body energy of the positronium antihydride $\bar{H}$Ps that appears in the final state. The such obtained effective potentials are presented in Fig. 4a, b.

We see that the effective interaction is purely attractive for the positron (Fig. 4a). But for the electron (Fig. 4b) it is repulsive at the origin (inside the positron cloud and close to the antiproton) but it is attractive at large distances, since the polarization effect is always attractive. We see also a small potential well present in the electron-core interaction (Fig. 4b), which is physically significant because the three body *negative* antihydrogen ion possesses weakly bound resonant states [32].

To test the effective interactions, we compare the binding energy of the antihydrogen ion $\bar{H}^+$ calculated with the core interactions (2-body problem, $E^{(2)}(\bar{H}^+) = -0.027717 a.u.$), with the exact coulombic 3-body problem ($E^{(3)}(\bar{H}^+) = -0.027717$ a.u.). The binding energies are the same up to 6 decimal digits. Similarly, the binding energy of the positronium antihydride $\bar{H}$Ps is the same when calculated with the core potentials (3-body problem, $E^{(3)}(\bar{H}\text{Ps}) = -0.039073$ a.u.), or as the exact Coulomb 4-body problem ($E^{(4)}(\bar{H}\text{Ps}) = -0.039073$ a.u.).

We thus see that the core-interactions work very well as far as the binding energy of the essential subclusters is concerned. But what can we tell about the wave functions? The wave functions are tested by the correlation functions, which are 1-dimensional probability densities. They are obtained from the total 4-body wave function Ψ by integrating out all coordinates except the one of interest

$$C_c(r_c) = \langle \Psi | \Psi \rangle_{\hat{\boldsymbol{r}}_c, \boldsymbol{R}_c, \boldsymbol{\rho}_c} \tag{9}$$

We stress that although the $C(r_c)$ depends on only one distance variable, it is obtained from the full 9-dimensional wave function written in 11 Jacobi coordinate sets (see Fig. 2) by means of transformations between these coordinate sets.

To test the quality of the wave functions obtained with the core potentials we investigate the probability density for finding a positron at the distance $r_{\bar{p}e^+}$ from the antiproton. The densities obtained with core potentials are compared to the ones obtained from the exact description of the system. Such comparison is performed both for $\bar{H}^+$ (left panel of Fig. 5) and for $\bar{H}$Ps (right panel of Fig. 5).

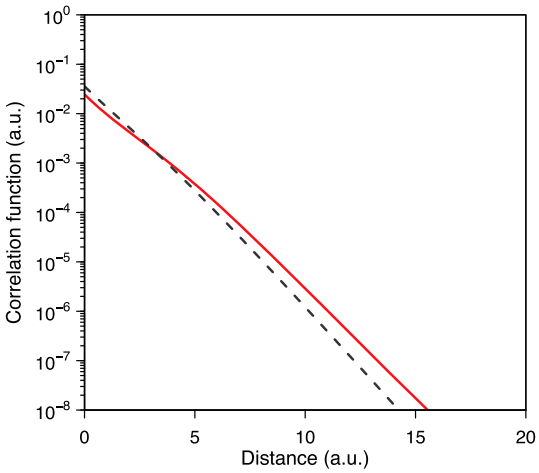

Fig. 6 The 1-dimensional probability density $C(r_{e^+e^-})$ for finding a positron at the distance $r_{e^+e^-}$ from the electron in $\bar{H}$Ps. The red solid line shows the probability density obtained from the exact 4-body solution for $\bar{H}$Ps, the broken line shows the same probability density obtained with the core potentials

The two panels of Fig. 5 show the probability of finding the positron at the distance $r_{\bar{p}e^+}$ from the antiproton, on the left for $\bar{H}^+$ and on the right for $\bar{H}$Ps. The circle-line shows the probability density obtained from the exact 3- and 4-body wave-functions (calculated with use of the exact 3 and 4 body Hamiltonians with strictly Coulombic inter-particle interactions). The other two lines show the same probability density obtained with the core potential that includes the polarization term (solid line), and without the polarization (dashed line). These densities are almost identical.

We also make similar test for the probability of finding the electron at the distance $r_{e^+e^-}$ from the positron. Figure 6 shows the correlation function $C(r_{e^+e^-})$ for $\bar{H}$Ps calculated with Coulomb interactions (red line) and with use of core interactions (broken line). We see that in the important region of strong correlation, i.e. at $r_{e^+e^-}$ distances on the order of 3 a.u. (the exact expectation value for the positron-electron distance in $\bar{H}$Ps is 3.48 a.u. [33]) the agreement of the two correlation functions is quite satisfactory.

Overall, the tests presented above show that the correlation functions obtained with core potentials agree quite well with the exact ones obtained with Coulomb potentials alone, which instills confidence in the quality of our wave functions for the $\mathrm{Ps} - \bar{H}^+$ system.

We then proceed to the calculation of the scattering cross sections.

5 Calculation of the Scattering Cross Sections

The cross sections for the reaction (1) are calculated by solving the Coupled Rearrangement Channel (CRC) problem using Gaussian Expansion Method (GEM) in Jacobi coordinates. Our CRC/GEM procedure involves two steps. First we solve the many-body Schrödinger equation for the entire scattering system as a matrix eigenvalue problem, using GEM. Next, we use the such obtained eigenfunctions as the many-body basis set for the construction of the inner part of the multi-channel scattering wave function, Ψ. The *inner part* of Ψ is expanded in terms of these eigenfunctions, and is augmented by the channel wave functions that satisfy the correct asymptotic boundary conditions in all scattering channels that are open at a given collision energy. Thus we write

$$\Psi = \Sigma_v b_v \Phi_v + \Sigma_\alpha \phi_\alpha . \tag{10}$$

In the above, Φ_v are the square integrable solutions to the 4-body Schrödinger equation, composed as in Eq. (3) and calculated for the 5-body Hamiltonian according to the frozen-core approach discussed in Sect. 4. ϕ_α are the (unknown) channel functions, their index α specifies the various possible fragmentations of the system, the internal states of the fragments, and the angular momentum of the relative motion of the fragments.

The channel functions ϕ_α contain the elements $S_{\beta,\alpha}$ of the scattering matrix **S** that are determined in the process of matching the channel functions to the inner part of the solution. The matching procedure is posed as a system of coupled, non-local integro-differential equations that determine self-consistently both the expansion

coefficients of the inner part of the scattering wave function (b_v in Eq. 10) *and* the channel functions that include the scattering matrix elements (functions ϕ_α in Eq. 10). These equations are solved using the Compact Difference Method. The details of the procedure are described in our work [23].

Once the elements of the scattering matrix $S_{\beta,\alpha}$ are obtained, they are used to calculate the channel to channel scattering cross sections $\sigma_{\beta,\alpha}$. The calculations are done separately for each total angular momentum J of the collisional system. It means that we solve the coupled channel equations for the multichannel scattering wave function Ψ of a given total angular momentum, and then use the J-dependent $S^{(J)}_{\beta,\alpha}$ in the suitably constructed partial wave expansions of the cross sections. The calculated cross sections of interest are given by

$$\sigma^{(\lambda_i)}_{\alpha,\alpha_i} = \frac{1}{k_i^2}(2\lambda_i + 1)|\delta_{\alpha,\alpha_i} - S^{(\lambda_i=J)}_{\alpha,\alpha_i}|^2, \qquad \sigma_{\mathcal{F}\mathcal{F}_i} = \sum_{\lambda_i} \sigma^{(\lambda_i)}_{\alpha,\alpha_i} \tag{11}$$

In the above, $\sigma^{(\lambda_i)}_{\alpha,\alpha_i}$ is the partial wave contribution to the state-to-state cross section $\sigma_{\mathcal{F}\mathcal{F}_i}$. The latter corresponds to the transition from a given fragmentation of the system $\mathcal{F}_i$ to another fragmentation $\mathcal{F}$. Since the fragments are in their ground states (the only existing bound states of $\bar{\mathrm{H}}^+$ and $\bar{\mathrm{H}}$Ps are the spin singlets with total internal angular momentum $\mathcal{L} = 0$) then the total angular momentum J of the collisional system is equal to the angular momentum of the relative motion ($\lambda_i = J$).

In the present calculation, the channels are numbered in the order of energy thresholds, i.e. $\alpha = 1$: $\bar{\mathrm{H}}$Ps$+e^+$, $\alpha = 2$: Ps $+ \bar{\mathrm{H}}^+$, $\alpha = 3$: $\bar{\mathrm{H}} +$ Ps$^+$. Thus, choosing the Ps $+ \bar{\mathrm{H}}^+$ as the initial state, for the collisional energy below the 3-body break-up the possible processes are: elastic scattering ($2 \to 2$), $\bar{\mathrm{H}}$Ps formation ($2 \to 1$) and Ps$^+$ formation ($2 \to 3$). We calculate the full scattering matrix, i.e. both the $S^{(J)}_{\alpha,\beta,}$ and the $S^{(J)}_{\beta,\alpha}$ matrix elements for the (time) reversed processes, without use of the detailed-balance theorem.

6 Results

The reactive disintegration of $\bar{\mathrm{H}}^+$ in Ps $+ \bar{\mathrm{H}}^+$ collisions is the result of two processes: production of the $\bar{\mathrm{H}}$Ps molecules and production of positronium ions Ps$^+$. Figure 7 shows the total cross section for reactive disintegration $\sigma_r = \sigma_{2,1} + \sigma_{2,3}$ (black full line), compared to the elastic scattering $\sigma_e = \sigma_{2,2}$ (black broken line). In addition, the figure shows the various partial contributions to these processes, classified by the total angular momentum J of the system, and by the spin-angular momentum of the two active positrons. The latter can be coupled either to $S^{e^+} = 0$ (situation referred to as "singlet scattering"), or to $S^{e^+} = 1$ (situation called "triplet scattering"). Spin coupling influences the spatial parity of the system, hence these two different situations result in different cross sections that in addition need to be premultiplied by the suitable spin-statistical factors: 1/4 for the singlet and 3/4 for the triplet scattering.

On Fig. 7 we see that for very low collisional energies (towards the Ps$+\bar{\mathrm{H}}^+$ threshold) the elastic scattering tends to a constant finite value but the inelastic scattering becomes huge, it diverges. The inelastic cross section has two components: formation of $\bar{\mathrm{H}}$Ps and formation of Ps$^+$. The divergence of inelastic scattering comes from the former contribution, more precisely from its $J = 0$ component (the other ($J > 0$) inelastic contributions tend to 0). This behavior confirms the general Wigner law ($\sigma_{21} \propto k^{2\lambda_i - 1}$).

The behavior of elastic scattering, in the presence of dispersive (polarization) interaction is expected to deviate from the Wigner's law for $J > 0$, but even if the standard power law ($\sigma_{22} \propto k^{4\lambda_i}$) is changed [34], it does not change the limiting values of the elastic cross sections at $E = 0$, i.e. $\sigma_{22}(0) =$ const for $J = 0$ and $\sigma_{22}(0) = 0$ for $J > 0$.

Looking at Fig. 7 we also observe that away from the threshold region (say for collisional energies $E > \simeq$ 0.01 a.u.) the elastic and inelastic cross sections become comparable. It means that the number of $\bar{\mathrm{H}}^+$ ions that are (elastically) scattered becomes about the same as the number of ions that undergo reaction. In other words roughly half of the $\bar{\mathrm{H}}^+$ ions are lost through inelastic collisions at $E > \simeq 0.01$ a.u.. As the ions thermalize via elastic collisions and their collisional energy drops below $E \simeq 0.01$ a.u., the inelastic collisions vastly exceed the elastic ones.

Regarding the spin we note that the Ps in the initial state can be either in spin singlet (ortho) or triplet state (para). The way that the positron spin of Ps couples to the positron spin of $\bar{\mathrm{H}}^+$ influences the spatial part of the scattering wave functions on account of the Pauli principle, so that, as seen on Fig. 7 there are two contributions to each partial wave cross section, depending on whether the positron spins couple to singlet or to triplet.

In $\bar{\mathrm{H}}^+ +$ Ps $\to \bar{\mathrm{H}}$Ps $+ e^+$ scattering, the two non-frozen positrons (one in Ps and the other in $\bar{\mathrm{H}}^+$) can couple freely to singlet or triplet and both situations will contribute, because the two non-frozen positrons of

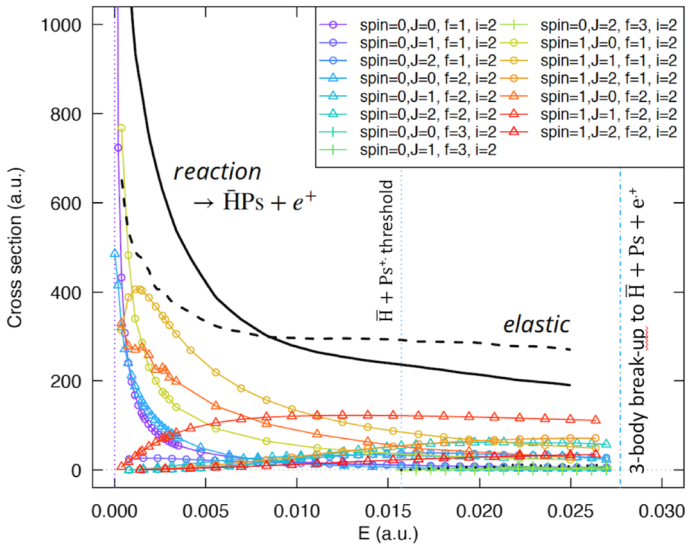

Fig. 7 The cross section for disintegration of $\bar{H}^+$: $\sigma_r = \sigma_{2,1} + \sigma_{2,3}$ (full black line) and for the elastic scattering: $\sigma_e = \sigma_{2,2}$ (dashed black line) in Ps + $\bar{H}^+$ collisions, as function of the collisional energy. The solid and broken black lines represent the cross sections that are summed over partial wave and spin contributions. The colored lines are partial wave cross sections (Eq. 11), premultiplied by the spin-statistical factors: 1/4 for positron singlet scattering and 3/4 for positron triplet scattering. Green triangles: spin singlet $S_{e^+} = 0$ partial contributions to the elastic scattering from $J = 0, 1, 2$. Red triangles: positron spin triplet $S_{e^+} = 1$ partial contributions to the elastic scattering from $J = 0, 1, 2$. Blue circles: positron spin singlet $S_{e^+} = 0$ partial contributions to the $\bar{H}$Ps formation from $J = 0, 1, 2$. Yellow circles: positron spin triplet $S_{e^+} = 1$ partial contributions to the $\bar{H}$Ps formation from $J = 0, 1, 2$. Light green bars: positron spin singlet $S_{e^+} = 0$ partial contributions to the Ps^+ formation from $J = 0, 1, 2$. The cross sections for Ps^+ formation are much smaller than those for the formation of $\bar{H}$Ps, and are barely visible in the scale of the graph. Ps^+ can not be formed in positron triplet state. The vertical dotted and dashed lines indicate the energy thresholds for Ps^+ formation and for the three-body break-up, respectively

the final state are not constrained to be in a specific spin state and can couple to either singlet or triplet. The situation is different for the $\bar{H}^+ + Ps \rightarrow \bar{H} + Ps^+$ scattering, since the Ps^+ formation channel does not open for triplet scattering. This is because of the spin constraint on the two active positrons in the initial state that must be coupled to a positron-singlet, since the bound state of Ps^+ in the final state exists only in the spin singlet state. Thus only singlet scattering is possible for this channel. This situation is similar to the $\bar{H} + Ps$ scattering resulting in bound $\bar{H}^+$ (see our work [23]). In that case, regardless if the initial Ps is in the *ortho* or *para* state only the spin states with two positrons (one on Ps and one on $\bar{H}$) coupled to the singlet can contribute, because two positrons in the final state *must* be coupled to the singlet if the $\bar{H}^+$ is to form a bound state.

7 Formation Versus Disintegration of $\bar{H}^+$ Ions

In the experiments at CERN [4–7], the $\bar{H}^+$ ions are to be obtained through collisions of the antihydrogen atoms passing through the stationary positron cloud according to the reaction

$$\bar{H} + Ps \rightarrow \bar{H}^+ + e^- . \tag{12}$$

Once formed, the $\bar{H}^+$ ions are moving in the same positron cloud in which they have been produced. It is therefore interesting to compare the scattering cross section of the formation reaction (12) with the depletion reaction (1).

Since the $\bar{H}^+$ ions are produced in $\bar{H} + Ps \rightarrow \bar{H}^+ + e^-$ collisions, the energy of newly produced $\bar{H}^+$ ions in the final state of reaction (12) is almost the same as the energy of $\bar{H}$ atoms in the initial state of this reaction. Because of the similar masses the outcoming $\bar{H}^+$ ions basically maintain the energy and momentum of the incoming $\bar{H}$ atoms (the outcoming products $\bar{H}^+$ maintain 99.89% of the lab energy of the incoming $\bar{H}$ projectiles). It is therefore interesting to compare the cross sections for disintegration and formation of $\bar{H}^+$ at the *same* collision energy.

Figure 8 shows the cross section for the formation reaction $\bar{H} + Ps \rightarrow \bar{H}^+ + e^-$ (σ_f) together with the cross section for the disintegration reaction $\bar{H}^+ + Ps \rightarrow \bar{H}Ps + e^+$ (σ_r). As discussed above, the calculation

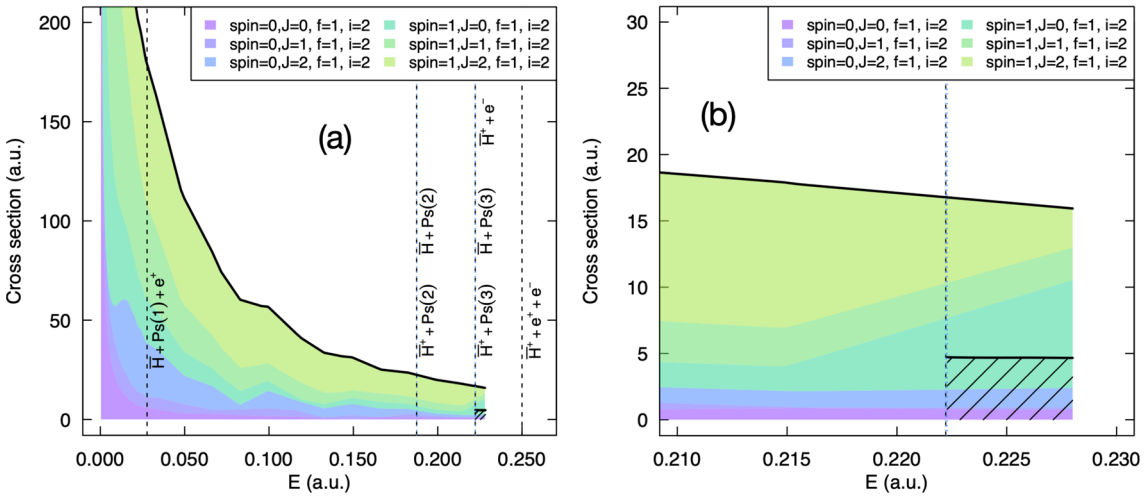

Fig. 8 The cross section for disintegration of $\bar{H}^+$ ($\sigma_r = \sigma_{2,1} + \sigma_{2,3}$, solid black line) shown together with the cross section for the formation of $\bar{H}^+$ (σ_f, solid black line above the striped area). The green and blue shades illustrate the partial wave contributions (Eq. 11) to the disintegration of $\bar{H}^+$ ions in positron singlet (blue) and positron triplet (green) scattering, respectively. Panel (a). The small striped area that starts at the threshold at $E = 0.2222$ a.u. shows the magnitude of the cross section for the formation of $\bar{H}^+$ in $\bar{H} + Ps$ collisions. The vertical dashed lines indicate various reaction thresholds. Panel (b). The magnification of the left panel allows better comparison of the cross sections for the formation of $\bar{H}^+$ (in $\bar{H} + Ps$ collisions) and its consecutive destruction (in $Ps + \bar{H}^+$ collisions). The latter is seen to be roughly 3 times larger than the former. The vertical dashed line shows the energy threshold for the formation of $\bar{H}^+$ ions in $Ps + \bar{H}$ collisions. The value of the formation cross section is taken from our work [23]. The statistical spin-factors are included in all presented cross sections

of the disintegration cross section σ_r includes all (3) channels that are open below the lowest threshold for the 3-body break-up in $\bar{H}^+ + Ps$ collisions (1), but not above it. The values of the formation cross section σ_f have been taken from our previous calculation [23] which includes all (7) channels that are open below the threshold for the formation reaction.

On Fig. 8a the color shades show accumulation of contributions to the disintegration cross section. The blue shades illustrate the partial wave contributions from scattering in positron spin singlet state; the green shades show partial wave contributions from scattering in positron spin triplet state. The cumulative sum of all contributions is depicted with the black solid line. Underneath, the small striped area shows the magnitude of the cross section for the formation of $\bar{H}^+$ in $\bar{H}(1s) + Ps(1s)$ collisions at the collisional energy just above what is needed for the formation reaction $\bar{H}(1s) + Ps(1s) \rightarrow \bar{H}^+ + e^-$ to take place (that is $E = 0.2222$ a.u., cf. Fig. 1).

Figure 8b shows the magnification of the cross sections for the formation and destruction of $\bar{H}^+$ ions, at collisional energies just above the threshold for reaction (12) (where the production cross section for $\bar{H}^+$ attains its maximum [35]). As is seen from Fig. 8b, close to the threshold for $\bar{H}^+$ formation the cross section for the loss of the $\bar{H}^+$ ions is roughly 3 times larger than the cross section for their formation.

In accordance with Wigner law for collisions ending with coulombically attracting fragments, the formation cross section σ_f starts with a finite value at the reaction threshold, and stays constant just above the threshold [23]. On the other hand, also in accordance with Wigner's prediction, the cross section for disintegration $\bar{H}^+ + Ps \rightarrow \bar{H}Ps + e^+$ (σ_r) diverges as $1/\sqrt{E}$ when $E \rightarrow 0$. At the energy sufficient for $\bar{H}^+$ formation, the disintegration is roughly 3 times larger than the formation (see Fig. 8). This factor rapidly grows as the newly formed $\bar{H}^+$ ion thermalizes in the Ps cloud, since, with the decreasing energy the elastic scattering tends to the finite value, but the destruction cross section rapidly increases (see Fig. 7), and finally diverges as $E \rightarrow 0$. For that reason, the experiments intending to harvest the $\bar{H}^+$ ions obtained through $\bar{H} + Ps$ collisions need a set-up that does not allow these ions to stay in the positronium target cloud too long.

8 Conclusions

We have elucidated the mechanism of the electron transfer during the collisional reaction $\bar{H}^+ + Ps \rightarrow \bar{H}Ps + e^+$. This has been done by the comparative study of the three dimensional, angle resolved positron density of the

free $\bar{H}^+$ in the initial state and the positron density of $\bar{H}$Ps in the final state. We could see that during the reaction the positron structure of $\bar{H}^+$ is largely maintained, however while embedded in $\bar{H}$Ps the $\bar{H}^+$ shrinks and gets more tightly bound as to generate the binding energy that is partly released be expelling the positron.

Guided by the insights from the density studies we have performed the first pilot calculation of the cross sections for the 5-body elastic and inelastic $\bar{H}^+ + Ps$ low energy collisions. For energies below the 3-body break-up two rearrangement processes can take place: formation of $\bar{H}$Ps atomcules and formation of Ps^+ ions. The cross sections for the latter process turned out to be much smaller than for the former so that the collisional loss of $\bar{H}^+$ ions is dominated by the formation of $\bar{H}$Ps. We have found that, in the limit of small collisional energies, the cross section for $\bar{H}$Ps formation diverges as $1/\sqrt{E}$, and the cross section for elastic scattering tends to the finite value.

We have also found that, assuming the same conditions of the target Ps cloud and the same collisional energy, the cross section for the loss of $\bar{H}^+$ ions in $\bar{H}^+ + Ps$ collisions (σ_r) is larger than the cross section for their formation in $\bar{H} + Ps$ collisions (σ_f). At collisional energies close to the threshold for $\bar{H}^+$ formation, the cross section for the subsequent loss of these ions (σ_r) is similar in size to the cross section for the elastic scattering σ_e, but it exceeds the cross section for the ion formation σ_f roughly by factor 3. As the $\bar{H}^+$ ions thermalize through Ps collisions, the ratio σ_r/σ_e increases rapidly since the cross section for ion loss diverges as $1/\sqrt{E}$ while the cross section for elastic collisions tends to the constant value.

Acknowledgements Piotr Froelich would like to thank Uppsala University for the support and research facilities. Svante Jonsell would like to thank the Swedish National Research Council (VR) for financial support. Takuma Yamashita and Yasushi Kino would like to thank JSPS KAKENHI Grant Number JP22K13980 and 18H05461.

Author contribution P.F. wrote the main manuscript and T.Y. performed the calculation and prepared figures. Y.K. and E.H. provided methods and part of codes. S.J. contributed to the formulation. All authors reviewed the manuscript.

Funding Open access funding provided by Uppsala University.

Data availability No datasets were generated or analysed during the current study.

Declarations

Conflict of interest The authors declare no competing interests.

References

1. A.M. Frolov, V.H. Smith, Phys. Rev. A **55**, 2662 (1997)
2. S. Bubin, K. Varga, Phys. Rev. A **84**, 012509 (2011)
3. S.L. Saito, Nucl. Instrum. Meth. Phys. Res. B **171**, 60 (2000)
4. G. Chardin et al. . Gbar, proposal to measure the gravitational behaviour of antihydrogen at rest, cern-spsc-p-342, 30/09/2011. Technical report (2011)
5. P. Indelicato et al., Hyperfine Interact. **228**, 141 (2014)
6. P. Perez et al., Hyp. Int. **233**, 21 (2015)
7. P. Adrich et al., Eur. Phys. J. C **83**(22), 1004 (2023)
8. L.D. Faddeev, Sov. Phys. JETP. **12**, 1014 (1961)
9. O.A. Yakubovsky, Sov. J. Nucl. Phys. **5**, 937 (1967)
10. E.O. Alt, P. Grassberger, W. Sandhas, Nucl. Phys. B **2**, 167 (1967)
11. A. Kievsky et al., J. Phys. G: Nucl. Part. Phys. **35**, 063101 (2008)
12. E. Hiyama, Y. Kino, M. Kamimura, Prog. Part. Nuclear Phys. **51**, 223 (2003)
13. R. Lazauskas, J. Carbonell, Phys. Rev. A **73**, 062717 (2006)
14. J. Carbonell, A. Deltuva, R. Lazauskas, Comptes Rendus. Physique **12**, 47 (2011)
15. R. Lazauskas, J. Carbonell, Front. Phys. **7**, 251 (2020)
16. R. Lazauskas, E. Hiyama, J. Carbonell. Phys. Rev. Lett. **130**, 102501 (2023)
17. E. Hiyama, M. Kamimura, Y. Yamamoto, T. Motoba, Phys. Rev. Lett. **104**, 212502 (2010)
18. E. Hiyama, A. Hosaka, M. Oka, J.-M. Richard, Phys. Rev. C **98**, 045208 (2018)
19. Y. Kino, N. Yamanaka, M. Kamimura, P. Froelich, H. Kudo, Hyperfine Interact. **138**, 179 (2001)

20. E. Hiyama, M. Kamimura, Few Body Syst. **54**, 1551 (2013)
21. M. Kamimura, Y. Kino, T. Yamashita, Phys. Rev. C **107**, 034607 (2023)
22. K. Piszczatowski, A. Voronin, P. Froelich, Phys. Rev. A **89**, 062703 (2014)
23. T. Yamashita, Y. Kino, E. Hiyama, S. Jonsell, P. Froelich, Phys. Rev. A **105**, 052812 (2022)
24. E. Hiyama, Prog. Theor. Exp. Phys. **2012**(1), 01A204 (2012)
25. E. Hiyama, M. Kamimura, Front. Phys. **13**(6), 132106 (2018)
26. M. Umair, S. Jonsell, Phys. Rev. A **92**, 012706 (2015)
27. M. Umair, S. Jonsell, Phys. Rev. A **93**, 052707 (2016)
28. M. Umair, S. Jonsell, J. Phys. B: At. Mol. Opt. Phys. **50**, 044001 (2017)
29. T. Yamashita, M. Umair, Y. Kino, J. Phys. B: Atom. Mol. Opt. Phys. **50**(20), 205002 (2017)
30. T. Yamashita, Y. Kino, Eur. Phys. J. D **72**(1), 13 (2018)
31. K. McDowell, J. Chem. Phys. **65**, 2518 (1976)
32. M. Umair, S. Jonsell, J. Phys. B: At. Mol. Opt. Phys. **47**(22), 225001 (2014)
33. J. Mitroy, Phys. Rev. A **73**, 054502 (2006)
34. H.R. Sadeghpour et al., J. Phys. B At. Mol. Opt. Phys. **33**, R93–R110 (2020)
35. P. Comini, P.-A. Hervieux, New J. Phys. **15**, 095022 (2013)